

# In Vitro Corrosion Anisotropy Assessment of Ti6Al4V Bimodal Microstructure due to Crystallographic Texture



MOHABBAT AMIRNEJAD, MOHAMMAD RAJABI, and ROOHOLLAH JAMAATI

The effect of crystallographic texture on the corrosion performance of the Ti6Al4V alloy with a typical bimodal microstructure has been studied on three orthogonal surfaces of the rectangular sample. The optical microscopy (OM) and scanning electron microscopy (SEM) observations revealed that the same microstructure is developed on three surfaces *via* heat treatment. The crystallographic planes, which are located in parallel to each surface, have been evaluated through macrotecture analysis. The electrochemical measurements showed that the RD-ND surface (*i.e.*, surface normal to transverse direction), in which  $\{0002\}$  and  $\{11\bar{2}0\}$  crystallographic planes are placed in parallel to the surface, has the lowest corrosion rate equal to  $2.2 \times 10^{-5}$  mm/year. In contrast, the corrosion rate of the TD-ND surface, which is normal to the rolling direction, with  $\{10\bar{1}0\}$  planes in parallel to the surface is  $\sim 15$  times greater than that of the RD-TD surface. Electrochemical impedance spectroscopy (EIS) results showed that the greater corrosion resistance of different surfaces is mainly dependent on the passive layer properties formed on each surface.

<https://doi.org/10.1007/s11661-021-06278-6>

© The Minerals, Metals & Materials Society and ASM International 2021

## I. INTRODUCTION

Ti6Al4V, as a dual-phase titanium alloy, has been used extensively as a metallic implant in the human body to restore a function by replacing or supporting a damaged structure.<sup>[1–4]</sup> In addition to the high strength to weight ratio, relatively low elastic modulus, inertness to the body environment, and enhanced biocompatibility, Ti6Al4V alloy possesses exceptional corrosion resistance in physiological solutions.<sup>[5–7]</sup> As an implant material, the corrosion behavior of Ti6Al4V alloy in human body fluids is of great importance. Despite the high corrosion resistance of Ti6Al4V alloy, which results from the spontaneous formation of a natural oxide layer on its surface,<sup>[8–10]</sup> it has been reported that the release of Al ions might cause diseases such as Alzheimer's disease.<sup>[11]</sup> Besides, vanadium toxicity has been reported in many studies.<sup>[12,13]</sup>

The crystallographic texture indicates the preferred orientation of grains in a polycrystalline material.<sup>[14]</sup> The importance of the crystallographic texture is due to the fact that many of the material's properties depend

on its texture. The effect of the crystallographic texture has been mainly investigated on the mechanical properties,<sup>[15–17]</sup> fracture behavior,<sup>[18]</sup> and fatigue behavior<sup>[19]</sup> of different metallic alloys. Concerning corrosion as a surface phenomenon, the properties of those crystallographic planes located in parallel to the exposed surfaces of the material can affect its corrosion behavior. To our knowledge, compared to the mechanical properties, few studies are available on the investigation of crystallographic texture effects on the corrosion performance of the metallic alloys, especially Ti6Al4V. The crystallographic texture effect on the corrosion properties of Mg-Nd-Zn alloy has been investigated by Tan *et al.*,<sup>[20]</sup> where the higher corrosion resistance of the basal texture has been reported.  $\{110\}$  Planes of Fe-17Cr ferritic stainless steel have been the most corrosion-resistant planes in the HNO<sub>3</sub> solution, as reported by Fu *et al.*<sup>[21]</sup> Martin *et al.*<sup>[22]</sup> reported that the corrosion resistance of Ti6Al4V alloy when the basal planes are parallel to the surface is lower than that of a surface parallel to prismatic planes. On the contrary, the higher corrosion resistance of titanium due to the preferred orientation of basal planes parallel to the surface has been reported by Chatterjee *et al.*<sup>[23]</sup>

Based on this background, it can be concluded that the investigation of the crystallographic orientation of the grains is mandatory to gain more insight into the corrosion behavior of a material. Reports on the effect of the crystallographic texture on the corrosion performance of Ti6Al4V alloy are lacking. Moreover, the

MOHABBAT AMIRNEJAD, MOHAMMAD RAJABI, and ROOHOLLAH JAMAATI are with the Department of Materials Engineering, Babol Noshirvani University of Technology, Shariati Ave., Babol 4714871167, Iran. Contact e-mail: m.rajabi@nit.ac.ir

Manuscript submitted February 3, 2021; accepted March 27, 2021.

Article published online April 24, 2021

reported inconsistencies related to the crystallographic texture effect on the corrosion performance of Ti6Al4V alloy may be attributable to the simultaneous impact of the texture and microstructure on the corrosion performance of the material. In our previous study, the effect of the basal plane orientation parallel to the exposed surface on the corrosion behavior of the alloy was investigated.<sup>[24]</sup> In contrast, the effect of other crystallographic planes was not determined. In the present study, aiming to investigate the effect of other crystallographic planes on the Ti6Al4V corrosion in phosphate-buffered saline (PBS) solution, regardless of its microstructure, it was planned to extend the study to develop different crystallographic textures using heat treatment in such a way that it would be possible to investigate the effect of plates on the corrosion of the alloy. For this purpose, a similar bimodal microstructure was created on three orthogonal surfaces of a rectangular sample, whereas different crystallographic planes are located parallel to each surface. In this way, the effect of the crystallographic texture on Ti6Al4V corrosion can be investigated independently from the microstructural features.

## II. MATERIALS AND METHODS

### A. Materials

A rolled Ti6Al4V alloy plate of 10 mm thickness (Alloy Supply, UK) with a chemical composition of 6.2 wt pct Al, 3.8 wt pct V, 0.05 wt pct Fe, 0.15 wt pct O, and 0.01 wt pct Mo with the balance of titanium was used as the raw material in this study. Rectangular samples, which were cut from as-received plate, with dimensions of 20 × 15 × 10 mm, were used for heat treatment in which the long axis of samples was parallel to the rolling direction. The presence of three orthogonal surfaces, namely TD-ND, RD-ND, and RD-TD, which are perpendicular to the rolling direction (RD), transverse direction (TD), and normal direction (ND), respectively, makes it possible to have distinct crystallographic planes in parallel to the surfaces of the same

microstructure. Figure 1(a) shows the 3D schematic illustration of samples. The  $\beta$ -transus temperature for this alloy was determined by soaking several samples at a temperature between 980 °C and 1000 °C (5 deg intervals) for 60 minutes, followed by water quenching. Given that, if the sample had reached the  $\beta$ -transus temperature, the quenched microstructure would be fully martensitic, the transition temperature was set to 995 °C. To provide the same microstructure for all surfaces, the samples were subjected to a solution treatment at the temperature of 954 °C for 1 hours, air cooled to room temperature, and then given a stabilization treatment at 700 °C for 2 hours, followed by air cooling, as depicted in Figure 1(b).

### B. Characterization

#### 1. Microstructure

The microstructural investigation was performed by the conventional metallographic procedure. Different surfaces, *i.e.*, TD-ND, RD-ND, and RD-TD surfaces, were ground by silicon carbide emery paper up to 2000 grit by wet grinding, followed by polishing with alumina of 0.3  $\mu\text{m}$ . The chemical etchant used was modified Kroll's reagent containing 20 mL HF, 10 mL HNO<sub>3</sub>, and 70 mL distilled water. The microstructure was examined using optical microscopy (OM, DG Victory-Dewinter optical microscope) and scanning electron microscopy (SEM, FEI ESEM QUANTA 200) equipped with 2017 EDAX EDS Silicon Drift detectors (SDDs). Quantitative analysis of microstructural features was conducted *via* Clemex Vision software.

#### 2. Crystallographic texture

Due to the limited volume fraction of  $\beta$  phase in Ti6Al4V alloy at room temperature, the macrotexture measurement was performed only for  $\alpha$  hexagonal phase (as a predominant phase) by x-ray diffraction method (XRD, PANalytical X-ray diffractometer) with Cr  $k_{\alpha}$  radiation ( $\lambda = 2.2936 \text{ \AA}$ ). A set of three incomplete pole figures including  $\{10\bar{1}0\}$ ,  $\{10\bar{1}1\}$ , and  $\{10\bar{1}3\}$  was measured for the heat-treated sample. The inverse pole

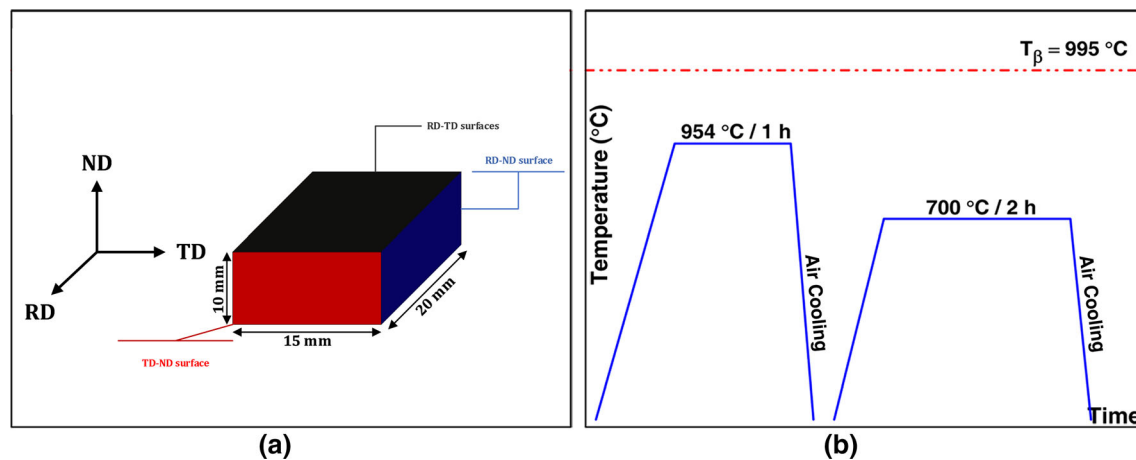


Fig. 1—(a) Rectangular sample illustration and (b) heat treatment schedule.

figures (IPFs) in normal, rolling, and transverse directions were calculated based on the orientation distribution function (ODF), calculated from the aforementioned incomplete pole figures. Calculations were performed using TexTools software (ResMat Co.).

### 3. Electrochemical evaluation

All electrochemical measurements were done using a potentiostat-galvanostat (VersaSTAT 4 equipped with a FRA/VersaSTAT4 impedance module) with a conventional three-electrode cell with a platinum sheet as the counter electrode, and standard calomel electrode (SCE,  $E_{deg} = +0.233 \text{ V vs SHE}$  at  $37 \text{ }^\circ\text{C}$ ) as the reference electrode. The polished surface of heat-treated Ti6Al4V with an exposed area of  $0.6 \text{ cm}^2$  was used as working electrode. The used electrolyte in this study was phosphate-buffered saline (PBS) solution composed of 8 g NaCl, 0.2 g  $\text{KH}_2\text{PO}_4$ , 2.9 g  $\text{Na}_2\text{HPO}_4$ , and 0.2 g KCl in 1000 mL of solution. All measurements were performed at  $37 \pm 1 \text{ }^\circ\text{C}$ . The open-circuit potential of each surface was monitored with time for 3600 seconds. The electrochemical impedance spectroscopy of samples was conducted by applying a 10 mV AC amplitude signal vs OCP over a frequency range of  $10^5$  to  $10^{-2}$  Hz. The electrochemical impedance spectroscopy (EIS) spectra have been displayed as Nyquist and Bode plots. EIS parameters were analyzed using ZView fitting software. Potentiodynamic polarization was applied from  $-0.25 \text{ V}$  in the cathodic direction to  $1.25 \text{ V}$  anodic potential vs OCP with a scan rate of  $1 \text{ mV/s}$ . All electrochemical measurements were made in triplicate for each surface, and the average results were reported. The morphological features of the corroded surface after the polarization test were investigated *via* SEM and EDS analysis.

## III. RESULTS

### A. Microstructure

Figures 2(a) through (c) shows the optical micrograph for RD-TD, TD-ND, and RD-ND surfaces and the corresponding equiaxed  $\alpha$  grain size distribution shown as inset histograms with a fitted normal distribution curve (line graph). As seen, the microstructures consist of equiaxed primary  $\alpha$  grains in a transformed  $\beta$  matrix, called a bimodal microstructure. Soaking the sample at  $954 \text{ }^\circ\text{C}$  for 60 minutes leads to the formation of the microstructure mainly composed of  $\beta$  phase, which is more stable at high temperatures, and a small number of globular  $\alpha$  grains within a  $\beta$  matrix. The globularization of primary  $\alpha$  grains is done to minimize the surface energy of  $\alpha$  grains.<sup>[25]</sup> During air cooling, the primary globular  $\alpha$  will grow to a certain extent. The high cooling rate through air cooling leads to the formation of a transformed  $\beta$  region (appears as an  $\alpha/\beta$  lamellar microstructure) within prior  $\beta$  grains. The second annealing step is performed at  $700 \text{ }^\circ\text{C}$  to stabilize the microstructure and release the internal stresses developed during air cooling from  $954 \text{ }^\circ\text{C}$ . The bimodal microstructure was selected for investigation in this study because it possesses a combination of strength, ductility, and good fatigue properties among different titanium microstructures and is, therefore, the most commonly used microstructure of Ti6Al4V alloy.<sup>[26]</sup> Image analysis was performed to quantify the microstructural features of different surfaces. The obtained results by statistical analysis are summarized in Table I.

As seen, the normal distribution curves for different surfaces are approximately congruent. The average primary  $\alpha$  grain sizes are  $6.08$ ,  $5.50$ , and  $5.37 \text{ }\mu\text{m}$  for RD-TD, TD-ND, and RD-ND surfaces, respectively.

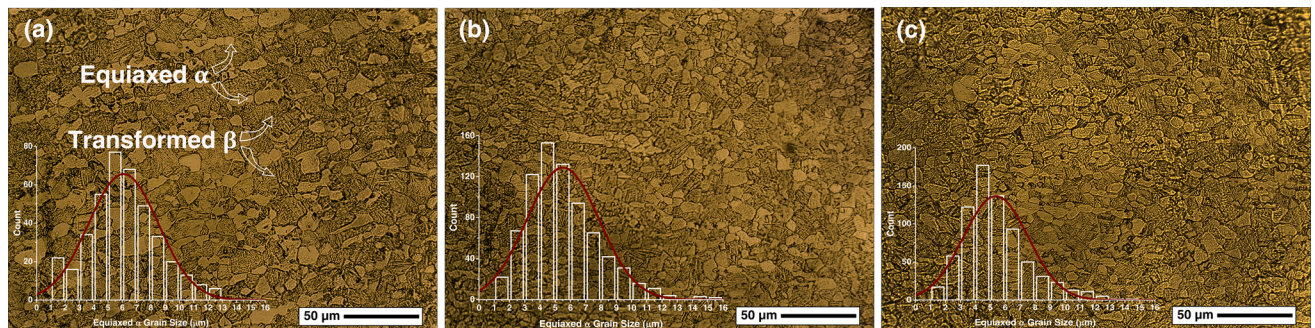


Fig. 2—The optical images of (a) RD-TD, (b) TD-ND, and (c) RD-ND surfaces along with corresponding grain size distribution (inset bar graphs).

Table I. Image Analysis Results for Different Surfaces

Surface	Average Grain Size ( $\mu\text{m}$ )	Standard Deviation ( $\mu\text{m}$ )	Standard Error ( $\mu\text{m}$ )	Equiaxed $\alpha$ Content (Pct)
RD-TD	6.08	2.44	0.121	29
TD-ND	5.50	2.37	0.089	36
RD-ND	5.37	2.16	0.079	31



The same standard deviation values (*i.e.*, 2.44, 2.37, and 2.16 for RD-TD, TD-ND, and RD-ND surfaces, respectively) represent a uniform spread out of equiaxed  $\alpha$  grain size. The majority of grains have a size between 4 and 7  $\mu\text{m}$  for all different surfaces. Moreover, the overall equiaxed  $\alpha$  grains for RD-TD, TD-ND, and RD-ND surfaces are equal to 29, 36, and 31 pct, respectively.

Figure 3 shows the heat-treated sample micrographs at different magnifications. The microstructure is a mixture of fine equiaxed primary  $\alpha$  grains surrounded by a transformed  $\beta$  matrix, as shown in Figure 3(a). It should be noted that transformed  $\beta$  regions were  $\beta$  phase at 954  $^{\circ}\text{C}$ , which transforms to a Widmanstatten microstructure during subsequent air cooling. The microstructure of the heat-treated sample at higher magnification is shown in Figure 3(b). It can be seen that the transformed  $\beta$  microstructure is mainly composed of Widmanstatten (lamellar) morphology.

The chemical composition disparity of the different microstructure constituents resulting from diffusional partitioning of alloying elements is shown in Figure 4. The vanadium content for the  $\beta$  phase, equiaxed  $\alpha$  phase, and  $\alpha$  lamellas is equal to 5.17, 1.98, and 3.24 wt pct, respectively. The  $\beta$  phase in transformed  $\beta$  microstructure is richer in vanadium compared to the  $\alpha$  phase with both equiaxed and lamellar morphology. The higher concentration of vanadium in  $\alpha$  lamellas in comparison to equiaxed  $\alpha$  grains may be ascribed to the diffusional partitioning rate of alloying elements. The

primary  $\alpha$  grain growth, with low vanadium content, which remains in the structure at 954  $^{\circ}\text{C}$ , leads to the formation of equiaxed  $\alpha$  morphology, whereas the plate-like  $\alpha$  grains form from a  $\beta$  parent phase with a high content of vanadium. During air cooling, there is not sufficient time to complete diffusional partitioning. It should be noted that for Ti6Al4V alloy, vanadium is a limiting element in the diffusional processes of the alloy.<sup>[27]</sup>

## B. Crystallographic Texture

The ODF of as-received Ti6Al4V alloy is presented in Figure 5, and the intensity distribution plots of the main fibers are illustrated in Figures 6(a) through (c). The  $\varphi_2 = 30$  deg section shows that two important fiber textures are present: the  $(11\bar{2}3) \perp \text{ND}$  fiber texture at  $\Phi = 45$  deg, which extends from  $\varphi_1 = 0$  deg to  $\varphi_1 = 360$  deg with an average intensity of 1.75 multiples of random distribution (mrd), and  $(11\bar{2}0) \perp \text{ND}$  fiber texture at  $\phi = 90$  deg and  $\varphi_1 = 0$  to 360 deg. The major component of  $(11\bar{2}3) \perp \text{ND}$  fiber is  $(11\bar{2}3)[1\bar{1}00]$  at  $\varphi_1 = 180$  deg,  $\Phi = 45$  deg, and  $\varphi_2 = 30$  deg with the intensity of 2.13 mrd (see Figures 5 and 6(a)). A certain uniformity is observed in  $(11\bar{2}0) \perp \text{ND}$  fiber intensity, as shown in Figure 6(b), with major texture components of  $(11\bar{2}0)[1\bar{1}00]$ ,  $(11\bar{2}0)[1\bar{1}02]$ ,  $(11\bar{2}0)[1\bar{1}01]$ , and  $(11\bar{2}0)[1\bar{1}0\bar{1}]$  with the intensity of 1.78, 1.84, 1.79, and 1.77 mrd, respectively. Moreover, a relatively weaker  $(01\bar{1}2) \perp \text{ND}$  fiber texture is seen at the  $\varphi_2 = 0$  deg section (see Figure 5) with an average intensity of 1.1 mrd with main texture components of  $(01\bar{1}2)[0001]$  and  $(01\bar{1}2)[22\bar{4}3]$  with the intensity of 1.25 and 1.14 mrd, respectively, as illustrated in Figure 6(c).

Figure 7 shows the ODF for the heat-treated sample. Contrary to the as-received material, no trace of fiber texture is observed in the heat-treated sample. The dominant texture components for the heat-treated Ti6Al4V alloy, along with their relevant characteristics, are summarized in Table II. During heat treatment, the crystallographic texture of the  $\alpha$  phase transforms from  $(11\bar{2}3) \perp \text{ND}$ ,  $(11\bar{2}0) \perp \text{ND}$ , and  $(01\bar{1}2) \perp \text{ND}$  fiber texture to  $\{01\bar{1}2\}22\bar{4}3$ ,  $\{01\bar{1}4\}2\bar{3}\bar{1}\bar{1}$ , and  $\{22\bar{3}1\}5\bar{4}\bar{1}\bar{1}$  components. The  $\{01\bar{1}2\}22\bar{4}3$  component with the intensity of 2.11 mrd is observed at  $\varphi_1 = 115$  deg,  $\Phi = 37$  deg, and  $\varphi_2 = 0$  deg, which is  $\sim 30$  deg away from  $\{0001\}22\bar{4}3$  orientation. The  $\{01\bar{1}4\}2\bar{3}\bar{1}\bar{1}$  component, which slightly tilted away from  $[0001] \parallel \text{ND}$  texture, appears at  $\varphi_1 = 230$  deg,  $\Phi = 25$  deg, and  $\varphi_2 = 0$  deg with the intensity of 1.92 mrd. Moreover, near the prismatic texture component  $\{22\bar{3}1\}5\bar{4}\bar{1}\bar{1}$  is the dominant texture component of the heat-treated sample with the 3.31 mrd.

During heat treatment, the simultaneous growth of prior  $\alpha$  grains and  $\alpha$  platelets in a Widmanstatten microstructure occurred. The crystallographic texture transformation during heat treatment can be caused by two mechanisms. The volume difference between the  $\alpha$  phase (with HCP structure) and the  $\beta$  phase (with BCC structure) causes stress in the structure during the phase

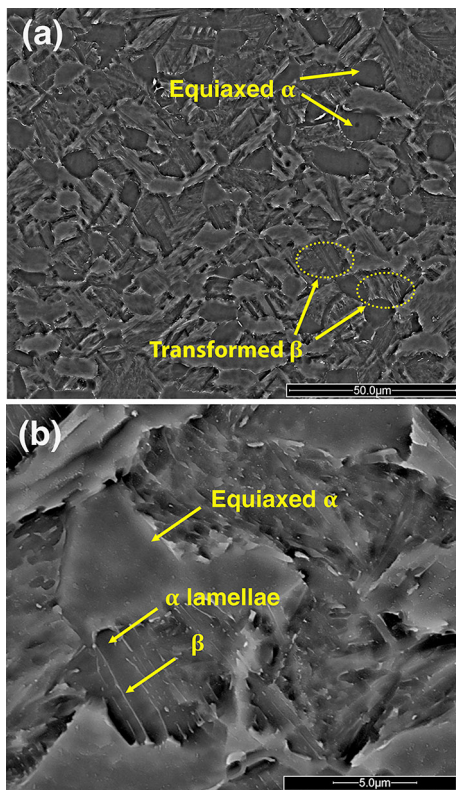


Fig. 3—SEM micrographs of bimodal Ti6Al4V microstructure at (a) low magnification and (b) high magnification.

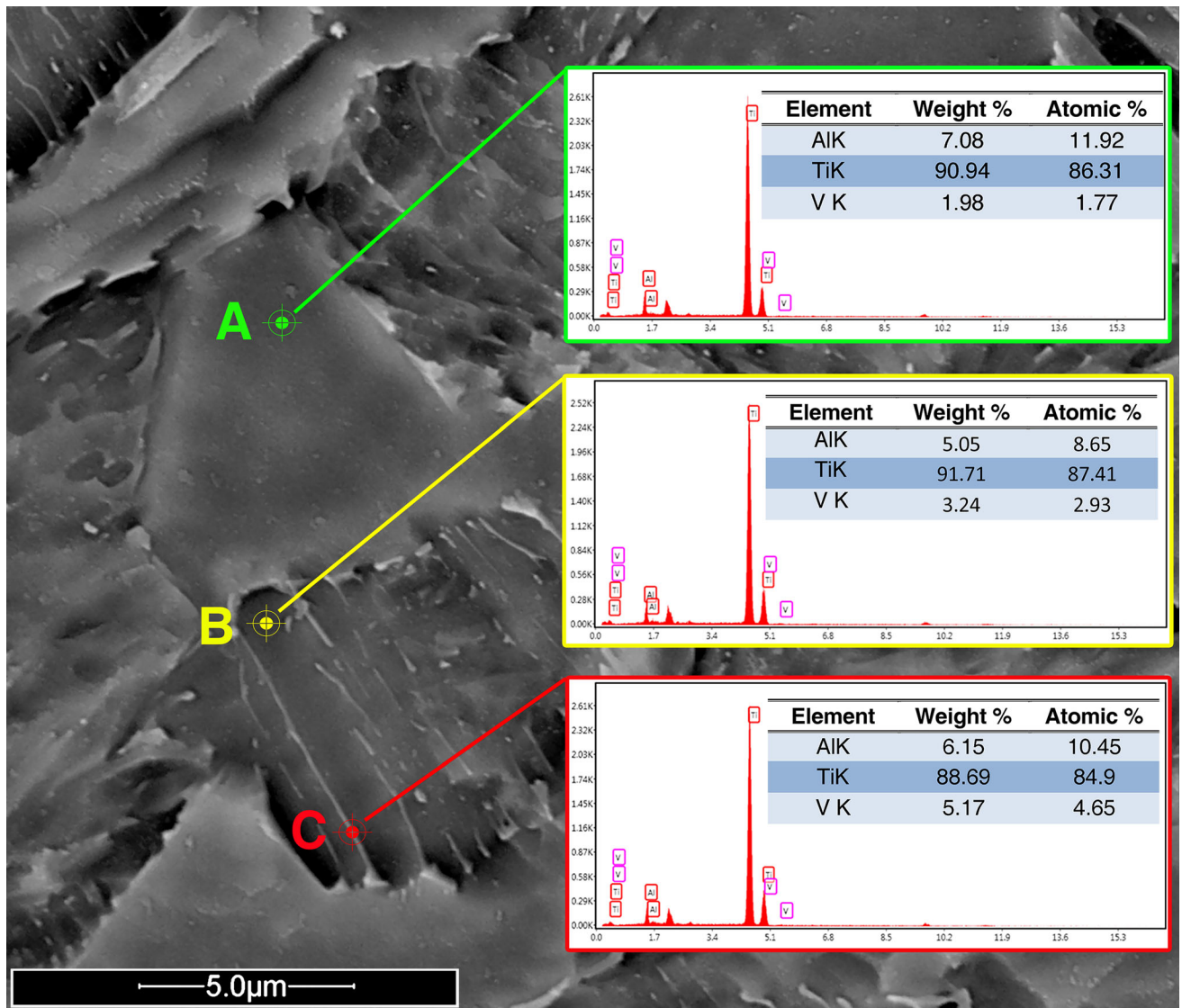


Fig. 4—EDS results for different microstructural constituents.

transformation. The variant selection during transformation would be changed as a result of stress, which can be effective on the formed  $\alpha$  phase texture.<sup>[28]</sup> Besides, it has been shown for Ti6Al4V alloy that the  $\alpha \leftrightarrow \beta$  phase transformation takes place according to an orientation relationship between  $\alpha$  and  $\beta$  phases called Burger's orientation relationship (BOR). The BOR can be explained as  $(0001)_{\alpha} \parallel (110)_{\beta}$  and  $11\bar{2}0_{\alpha} \parallel 1\bar{1}1_{\beta}$ . The nucleation and growth of  $\alpha$  platelets from the parent  $\beta$  phase based on BOR will lead to the change in as-received material crystallographic texture during heat treatment.<sup>[28,29]</sup>

Corrosion reactions usually occur on the surface of the alloy. Therefore, for a better understanding of the crystallographic texture effect on corrosion characteristics, it is necessary to identify the crystallographic planes that are located in parallel to the surfaces that undergo

the corrosion reactions. Inverse pole figures are used for this purpose. The crystallographic texture of the  $\alpha$  phase in the heat-treated sample is presented by IPFs (Figure 8). The inverse pole figure corresponding to ND shows high axis densities located around the  $[10\bar{1}4]$  direction with the intensity of 1.3 mrd. The maximum intensity location implies that basal planes of many grains are oriented at  $\sim 15$  deg to the RD-TD surface. Furthermore, the  $[20\bar{2}1]$  direction of some grains is parallel to ND. The IPF of RD shows the  $10\bar{1}0 \parallel$  RD texture with a maximum intensity of 1.31 mrd, where many grains have their  $\{10\bar{1}0\}$  planes in parallel to the TD-ND surface. Finally, the inverse pole figure of TD shows more scattered high axis densities around  $11\bar{2}1$  with an intensity of 1.20 mrd as well as  $10\bar{1}6$  with a maximum intensity of 1.17 mrd. It can be concluded



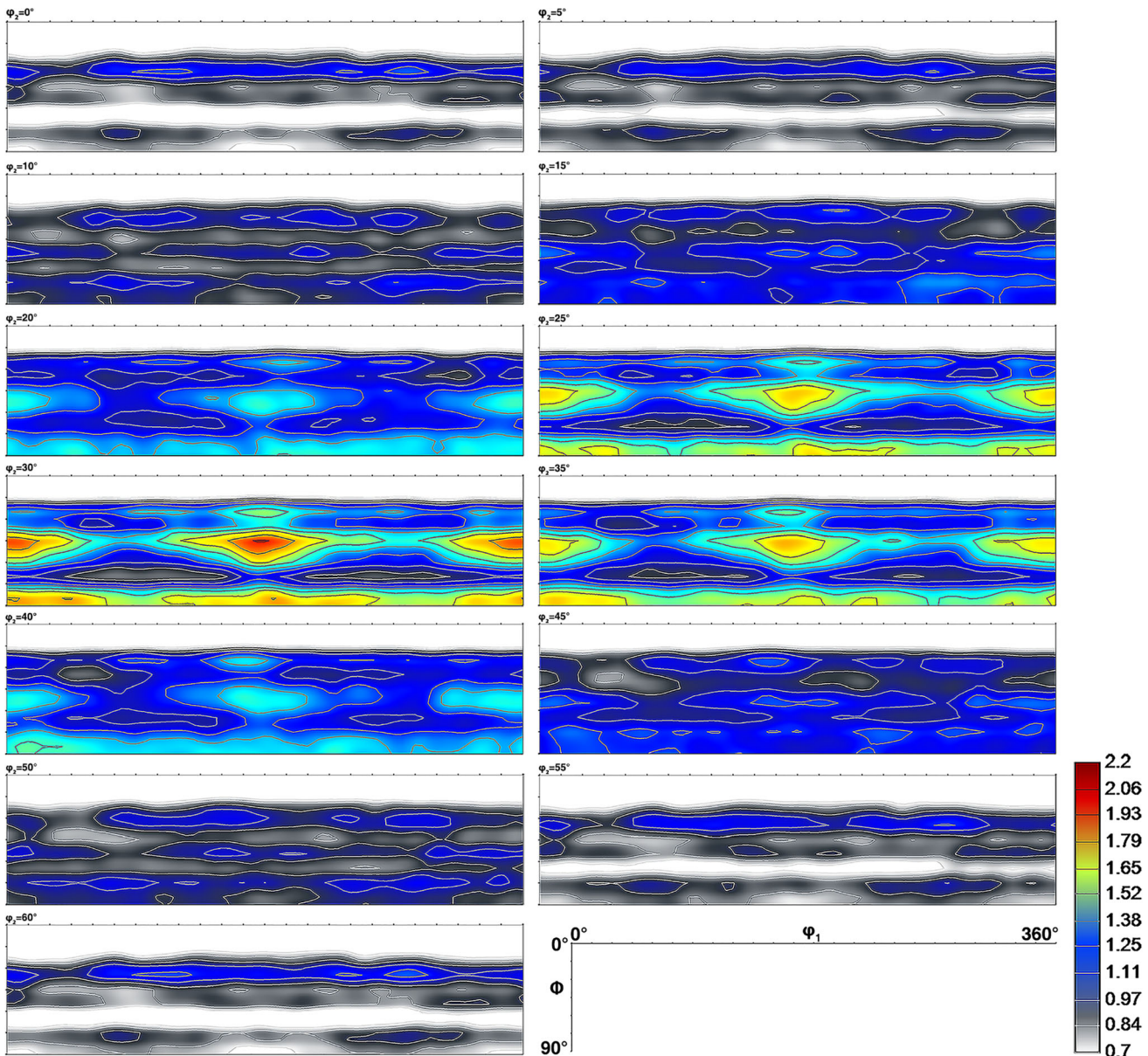


Fig. 5—ODF of as-received Ti6Al4V alloy.

that the  $11\bar{2}0$  direction of many grains was nearly parallel to TD. Moreover, the 0001 directions of some grains were found to be approximately parallel to TD.

### C. Electrochemical Evaluation

#### 1. Open circuit potential (OCP)

The OCP variation during 1 hours in PBS solution is presented in Figure 9 for three orthogonal surfaces of the sample. The positive shift in OCP values is observed for all three surfaces, which can be ascribed to the decrease of anodic reaction kinetics as a result of natural oxide film formation on the exposed surface during immersion time.<sup>[30]</sup> The natural oxide film formation leads to a thermodynamic equilibrium between anodic and cathodic reactions occurring on different surfaces, showing itself by OCP stabilization after 1 hours

immersion. It should be noted that in oxidizing environments, a compact and coherent oxide film with a thickness of about 2 nm, which mainly contains  $\text{TiO}_2$ , is spontaneously formed on the titanium alloy surface.<sup>[31–33]</sup> This oxide layer can impede corrosion by preventing the dissolution of metallic ions.<sup>[34]</sup>

#### 2. Potentiodynamic polarization

The corrosion performance of RD-TD, TD-ND, and RD-ND surfaces was investigated by potentiodynamic polarization test. Figure 10(a) shows the polarization curve of different surfaces of heat-treated alloy in PBS solution. The calculated corrosion parameters based on Tafel extrapolation, namely the corrosion potential ( $E_{\text{corr}}$ ), corrosion current density ( $i_{\text{corr}}$ ), and corresponding Tafel slopes, are summarized in Table III, along with the passive current density ( $i_{\text{pass}}$ ). Moreover, the

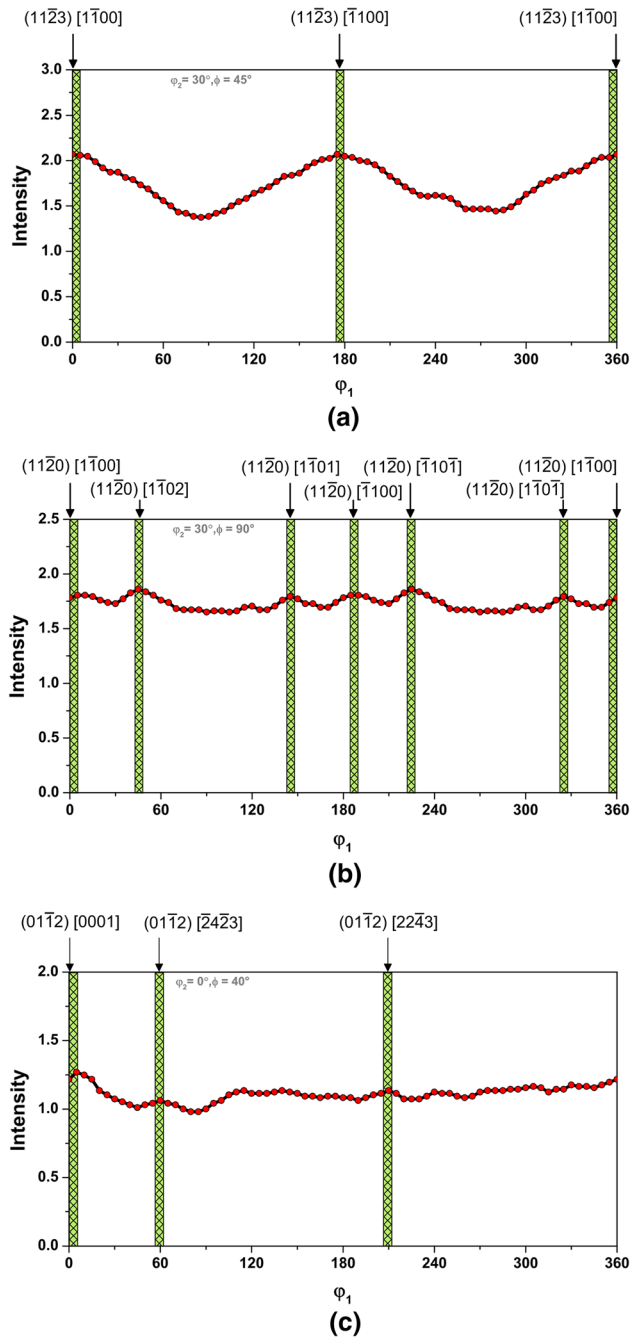


Fig. 6—Skeleton lines (intensity vs  $\phi_1$ ) of ODF represented at (a)  $\phi_2 = 30$  deg and  $\phi = 45$  deg, (b)  $\phi_2 = 30$  deg and  $\phi = 90$  deg, and (c)  $\phi_2 = 0$  deg and  $\phi = 40$  deg for as-received material.

calculated corrosion rates for three different surfaces are illustrated in Figure 10(b). Faraday's law was used to calculate the corrosion rates, according to ASTM G102-89<sup>[35]</sup>:

$$\text{Corrosion rate (mm/year)} = K \times i_{\text{corr}} \times EW/\rho \quad [1]$$

where  $EW$  stands for equivalent weight and is equal to 11.768 for Ti6Al4V alloy,  $i_{\text{corr}}$  is the corrosion current density in  $\mu\text{A}/\text{cm}^2$ ,  $K = 3.27 \times 10^{-3}$  mm g/ $\mu\text{A cm y}$ , and  $\rho$  is density in g/ $\text{cm}^3$ .

The corrosion potentials of RD-TD, TD-ND, and RD-ND surfaces are  $-0.501 \pm 0.08$  V,  $-0.083 \pm 0.03$  V, and  $-0.294 \pm 0.06$  V vs SCE, respectively, which are in good agreement with the OCP results. The TD-ND surface has the highest corrosion current density equal to  $37.4 \pm 2.4$  nA/ $\text{cm}^2$ , whereas the RD-ND surface reveals the lowest corrosion current density of  $2.25 \pm 0.8$  nA/ $\text{cm}^2$ . The corrosion current density measured at the RD-TD surface was  $8.3 \pm 1.2$  nA/ $\text{cm}^2$ . As seen in Figure 10(a), an apparent passive plateau was observed for the RD-TD and RD-ND surfaces in which the current density remains constant over a range of potential. However, this is not the case for the TD-ND surface, where the current density is continuously increased with increasing applied potential, and no specific passivation region is observed. This suggests that the TD-ND passivation ability is lower than the other two surfaces. The passive plateau for the RD-TD surface starts at  $-0.136$  V and ends around  $0.049$  V, whereas the RD-ND surface exhibits the potential range of the passive region from  $0.427$  to  $0.776$  V. The passivation current density of the RD-ND surface is lower than that of the RD-TD surface (see Table III) demonstrating that the protective efficiency of the passive film formed on the RD-ND surface is more significant in comparison with that of the RD-TD surface. The small increase of current density by increasing the potential to values higher than the end potential of the passive region, as seen for polarization curves of RD-TD and RD-ND surfaces in Figure 10(a), can be attributed to the partial degradation of the passive film.<sup>[36]</sup>

The corrosion resistance of metallic biomaterials is essentially dependent on their passivation ability.<sup>[37]</sup> According to Eq. [1], the corrosion rate of different surfaces is proportional to their corrosion current densities. The corrosion rate of three surfaces is graded below (shown in Figure 10(b)):

$$\text{CR(RD-ND)} < \text{CR (RD-TD)} < \text{CR (TD-ND)} \quad [2]$$

These results are consistent with the results obtained for the passivation ability of different surfaces (see Table III). Moreover, Videla *et al.*<sup>[38]</sup> have reported that to prevent surrounding tissue from damage or irritation, the metallic biomaterial corrosion rate should be  $< 2.5 \times 10^{-4}$  mm/year. The acceptable corrosion rate (ACR) of a metallic implant is shown as the ACR (green) bar in Figure 10(b). Based on the obtained results, the corrosion rate of the TD-ND surface is around 36 pct higher than the acceptable corrosion rate.

### 3. Electrochemical impedance spectroscopy

The EIS, as a nondestructive method, is used to investigate the mechanism of metallic implant corrosion in physiological environments. Figure 11 shows the experimental (symbols) and fitted (continuous line) Nyquist plot [impedance imaginary part ( $Z''$ ) vs real part of impedance ( $Z'$ )] as well as Bode plots [module  $|z|$  and phase angle vs. frequency (Hz)] for different surfaces of heat-treated Ti6Al4V in PBS solution.



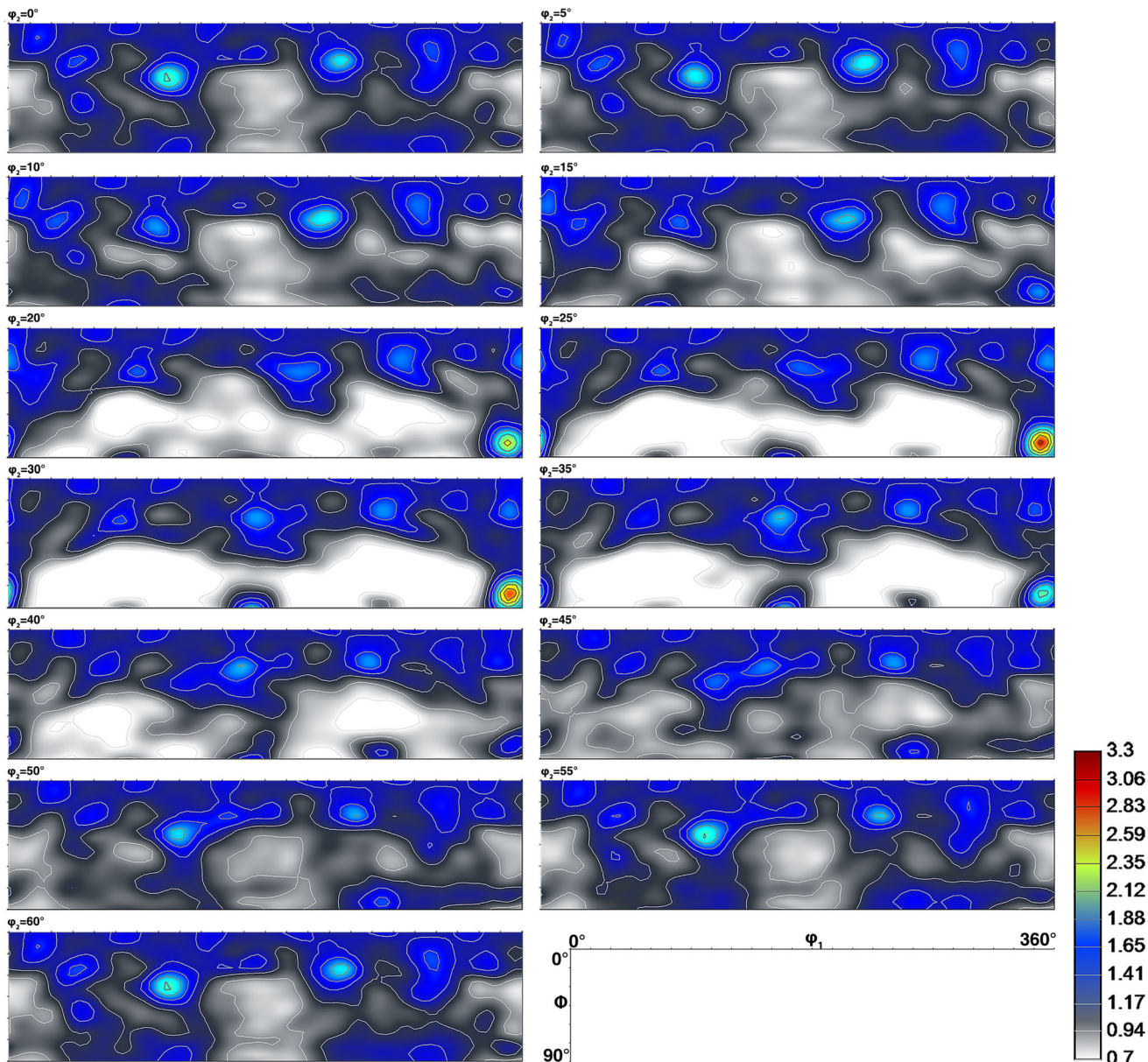


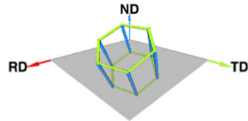
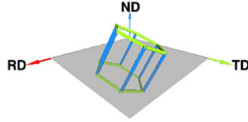
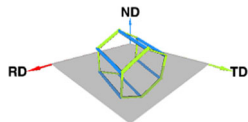
Fig. 7—ODF of the heat-treated Ti6Al4V alloy.

Blackwood<sup>[39]</sup> showed that the semiconductor nature of the titanium oxide layer should be taken into consideration when interpreting EIS results. According to this, the EIS spectra were fitted by an  $R_S + CPE_{SC}/R_{SC} + C_b/R_b$  electrical equivalent circuit (Figure 11(a), inset) where  $R_S$  stands for the solution resistance,  $CPE_{SC}$  and  $R_{SC}$  are the capacitance and resistance of the space-charge region (SCR),  $R_b$  is the resistance of the oxide barrier layer, and  $C_b$  represents the capacitance of the compact oxide layer. It should be stated that the bending of valence and conduction bands on the surface of the titanium oxide, as an n-type semiconductor, at a positive polarization, leads to the formation of the space-charge region (SCR) at the interface between the oxide film and electrolyte.<sup>[40]</sup> This electrical equivalent circuit has also been used by Poznyak *et al.*<sup>[41]</sup> to

investigate the mechanisms involved in Ti alloy corrosion. The constant phase element with the impedance of  $Z_{CPE} = 1/Y_0(j\omega)^n$  is used instead of the ideal capacitor due to the inhomogeneous surfaces of the natural oxide layer and Ti6Al4V alloy itself.<sup>[42]</sup>  $Y_0$  is the constant phase element admittance,  $j = \sqrt{-1}$ ,  $\omega$  is the angular frequency of AC voltage, and  $n$  is the constant phase element exponent ranging from 0 for a pure resistance to 1 for a pure capacitance behavior of CPE. The  $n$  value for the barrier layer as a constant phase element was calculated to be equal to  $\sim 0.99$ . As a result, the CPE element of the barrier oxide resembles an ideal capacitance ( $n = 1$ ). The relevant fitted values are summarized in Table IV. It can be concluded from the low chi-squared ( $\chi^2$ ) values that the used electrical



**Table II. Major Texture Component Characteristics**

Component	Euler Angles (Deg)			Intensity (mrd)	Crystal Orientation
	$\varphi_1$	$\Phi$	$\varphi_2$		
$\{01\bar{1}2\}\bar{2}243$	115	37	0	2.11	
$\{01\bar{1}4\}\bar{2}3\bar{1}\bar{1}$	230	25	0	1.92	
$\{2\bar{2}41\}54\bar{1}\bar{1}$	350	82	25	3.31	

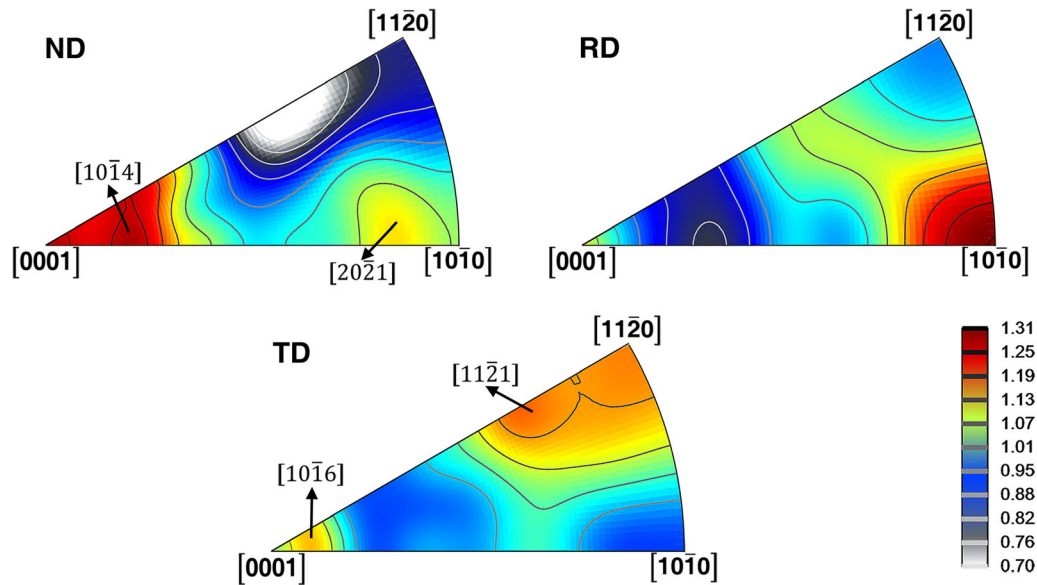


Fig. 8—IPFs of the heat-treated sample.

equivalent circuit can properly represent the surfaces' response to AC voltage.

As shown in Figure 11(a), the RD-ND surface has the highest semicircular diameter in the Nyquist curve, indicating that the RD-ND surface has a higher corrosion resistance than other surfaces, as already determined by potentiodynamic polarization results (Figure 10). The constant values of  $|Z|$  at high frequencies in Bode plots are related to the uncompensated solution resistance. The results (see Figure 11 and Table IV) show that solution resistances are nearly the same for all three surfaces. This can be attributed to the infinite amount of electrolyte, whose resistance cannot

be affected by the small variation in the released metallic ion concentration. For all surfaces, approaching the phase angle values to 90 deg at medium to low frequencies could be ascribed to the formation of a stable passive layer on all surfaces.<sup>[36]</sup>

The thickness of the oxide barrier layer, as an effective layer for providing corrosion resistance, is inversely proportional to its capacitance value, such as given below<sup>[43]</sup>:

$$d = (1/C)(\epsilon_0 \epsilon_r A) \quad [3]$$

where  $\epsilon_0 = 8.85 \times 10^{-14} \text{ Fcm}^{-1}$  is the permittivity of the vacuum,  $\epsilon_r$  is the relative permittivity of the oxide film

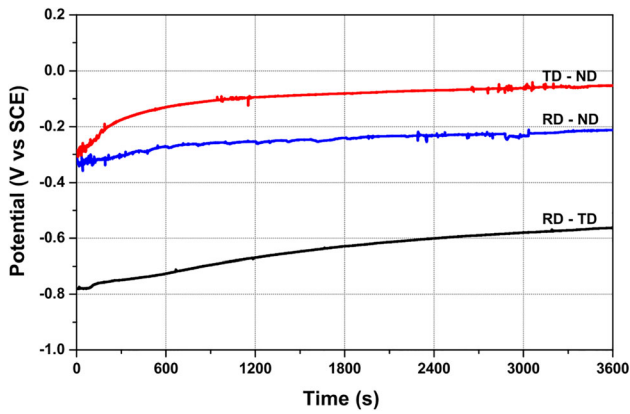


Fig. 9—OCP evaluation of three different surfaces in PBS solution.

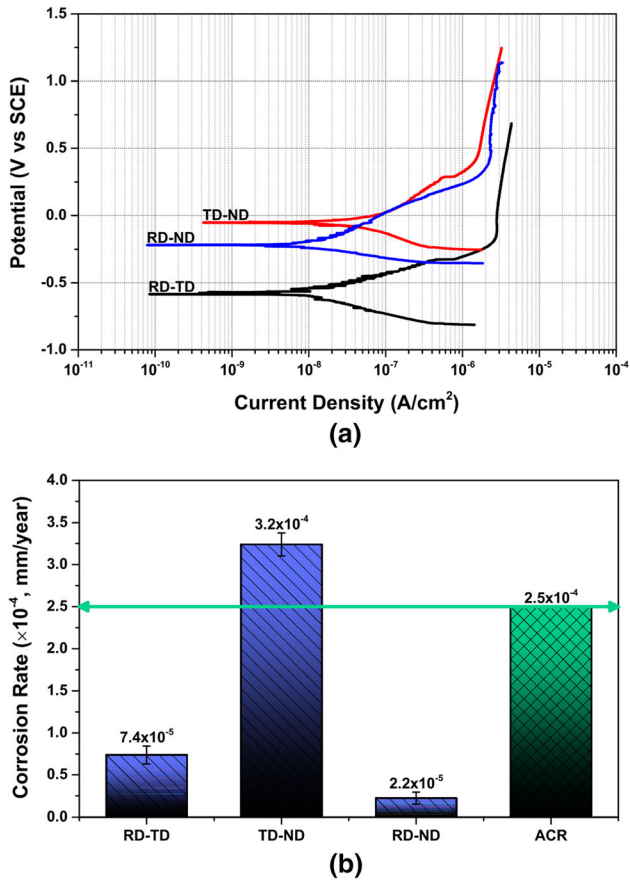


Fig. 10—(a) Potentiodynamic polarization curves and (b) corrosion rates for different surfaces of the heat-treated sample.

(generally considered to be equal to 100 for titanium oxide<sup>[44]</sup>), and  $A$  is the surface area, which was equal to  $0.6 \text{ cm}^2$  in this study.

Figure 12 shows the obtained  $C_b$  and corresponding  $d$  values for RD-TD, TD-ND, and RD-ND surfaces. To obtain better insight into the effect of barrier layer thickness on corrosion resistance, the corrosion rate of different surfaces is also presented in Figure 12 as bar graphs. The  $C_b$  values for RD-ND, RD-TD, and TD-ND surfaces were calculated to be 18.5, 29.4, and

$41.6 \mu\text{F cm}^{-2}$ , respectively, and the corresponding inner barrier layer thicknesses were found to be  $2.88 \pm 0.26$ ,  $1.80 \pm 0.09$ , and  $1.27 \pm 0.01 \text{ nm}$ , respectively. Moreover, the results indicate a direct relationship between the natural oxide layer thickness and the resistance to corrosion for different surfaces. The RD-ND surface with a barrier layer thickness of  $2.88 \pm 0.26 \text{ nm}$  showed the highest corrosion resistance with a corrosion rate of  $2.2 \times 10^{-5} \text{ mm/year}$  compared to other surfaces. The decrease in oxide layer thickness to  $1.27 \pm 0.01 \text{ nm}$  for the TD-ND surface increases the corresponding corrosion rate to  $3.2 \times 10^{-4} \text{ mm/year}$ .

#### D. Corrosion Surface Morphology

Figure 13(a) through (c) shows the SEM images of the RD-TD, TD-ND, and RD-ND surfaces after a polarization test in the PBS solution. Furthermore, the corroded surfaces were chemically analyzed by the EDS plane scan as represented in Figures 13(d) through (g). The results show that a uniform layer was formed on the RD-TD and RD-ND surfaces (Figures 13(a) through (c)), whereas, a large number of corrosion products were accumulated on TD-ND surface as shown at low magnification and higher magnification (inset) in Figure 13(b). The corresponding EDS plane scan (Figure 13(e)) revealed that these clusters contain a noticeable oxygen content of around 17.5 wt pct. The existence of oxygen and titanium accompanied by aluminum and vanadium peaks could indicate that the formed passive layer on all three surfaces, in addition to titanium oxide, also contains aluminum and vanadium oxides. Besides, according to EDS analysis, the increasing order of oxygen content in corrosion layers is as follows:

$$\text{TD-ND} > \text{RD-TD} > \text{RD-ND} \quad [4]$$

Higher levels of oxygen in the corroded surfaces may imply that larger amounts of corrosion products have formed on the surface as a result of higher corrosion rates. Accordingly, there is good agreement between the relative amount of oxygen on the corroded surfaces and the corresponding corrosion rates shown in Figure 10.

## IV. DISCUSSION

All three surfaces have the same microstructural features (Figure 2). Therefore, the corrosion performance of different surfaces can exclusively be affected by the crystallographic orientations, especially the crystallographic planes placed parallel to the exposed surface. It was observed that the RD-ND surface in which the  $\{0002\}$  planes of some grains and  $\{11\bar{2}0\}$  planes of some other grains are nearly parallel to the exposed surface exhibits the most excellent corrosion resistance among all three surfaces. On the contrary, the lowest corrosion resistance belongs to the TD-ND surface, where many grains are oriented in such a way that their  $\{10\bar{1}0\}$  prismatic planes are located nearly parallel to



**Table III. Corrosion Parameters of RD-TD, TD-ND, and RD-ND Surfaces Calculated by Tafel Extrapolation Method**

Surface	$E_{\text{corr}}$ (V vs. SCE)	$i_{\text{corr}}$ (nA/cm <sup>2</sup> )	$i_{\text{pass}}$ (μA/cm <sup>2</sup> )	Corrosion Rate ( $\times 10^{-4}$ , mm/year)
RD-TD	$0.501 \pm 0.08$	$8.3 \pm 1.2$	2.80	$0.74 \pm 0.10$
TD-ND	$-0.083 \pm 0.03$	$37.4 \pm 2.4$	—	$3.4 \pm 0.14$
RD-ND	$-0.294 \pm 0.06$	$2.25 \pm 0.8$	2.33	$0.22 \pm 0.07$

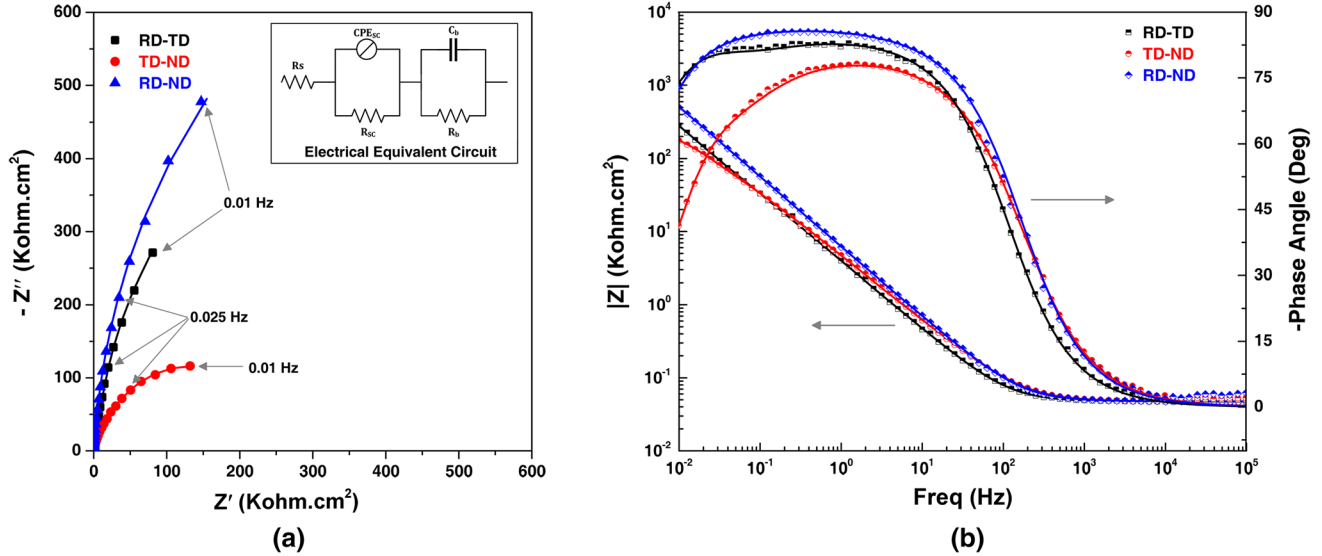


Fig. 11—EIS spectra for RD-TD, TD-ND, and RD-ND surfaces in PBS solution: (a) Nyquist plot with the equivalent circuit (inset) and (b) Bode plots.

**Table IV. EIS Fitting Parameters**

Surface	$R_s$ ( $\Omega \text{ cm}^2$ )	$R_{sc}$ ( $\text{K}\Omega \text{ cm}^2$ )	$CPE_{sc}$ ( $\mu\text{F cm}^{-2}\text{s}^{n-1}$ )	$n$	$R_b$ ( $\text{M}\Omega \text{ cm}^2$ )	$C_b$ ( $\mu\text{F cm}^{-2}$ )	$\chi^2 \times 10^{-3}$
RD-TD	$71.1 \pm 14.6$	$16.3 \pm 6.4$	$79.7 \pm 18.8$	0.82	$1.76 \pm 0.3$	$29.4 \pm 1.5$	< 4
TD-ND	$64.0 \pm 21.9$	$51.5 \pm 3.7$	$38.2 \pm 6.7$	0.84	$0.43 \pm 0.03$	$41.6 \pm 0.4$	< 1
RD-ND	$76.6 \pm 9.6$	$172.0 \pm 39$	$87.3 \pm 31$	0.79	$3.06 \pm 0.1$	$18.5 \pm 1.7$	< 2

the corroding surface. The measured corrosion rate for the RD-TD surface, wherein {0002} planes of many grains and {10 $\bar{1}$ 0} planes of some grains are placed nearly parallel to the surface, has a certain value between the corrosion rate of RD-ND and TD-ND surfaces. It seems that the {10 $\bar{1}$ 0} planes are the most prone to corrosion, whereas the orientation of {0002} and {11 $\bar{2}$ 0} planes in parallel to the RD-ND surface will lead to the highest corrosion resistance.

It should be mentioned that the {0002} planes in the hcp structure are closed-pack planes that have a higher atomic planar density compared to other crystallographic planes. Besides, the higher binding energy of these planes has been identified, as well as the higher dissolution activation energy barrier, as to other planes in hcp. It is possible to deduce that the {0002} close-packed planes would have the highest corrosion resistance of all other hcp planes. It was shown in our

previous study<sup>[24]</sup> that the surface in which many grains have their basal planes parallel to the surface offers greater corrosion resistance in comparison with the surfaces of more scattered crystallographic texture at the same microstructure. The lower corrosion rate of high-density planes in comparison to that of planes with lower planar density has also been reported by Shahryari *et al.*<sup>[45]</sup> They showed that the basal planes of pure titanium single crystal provide better corrosion resistance than the (11 $\bar{2}$ 0) and (10 $\bar{1}$ 0) planes.

On the other hand, the electrochemical measurements revealed that the corrosion resistance of different surfaces is primarily dependent on the formed passive layer properties. The excellent corrosion resistance of titanium and its alloys is mainly due to titanium's high reactivity with oxygen, leading to the rapid formation of a stable oxide layer.<sup>[46–48]</sup> The highest corrosion resistance of the RD-ND surface can be attributed to the

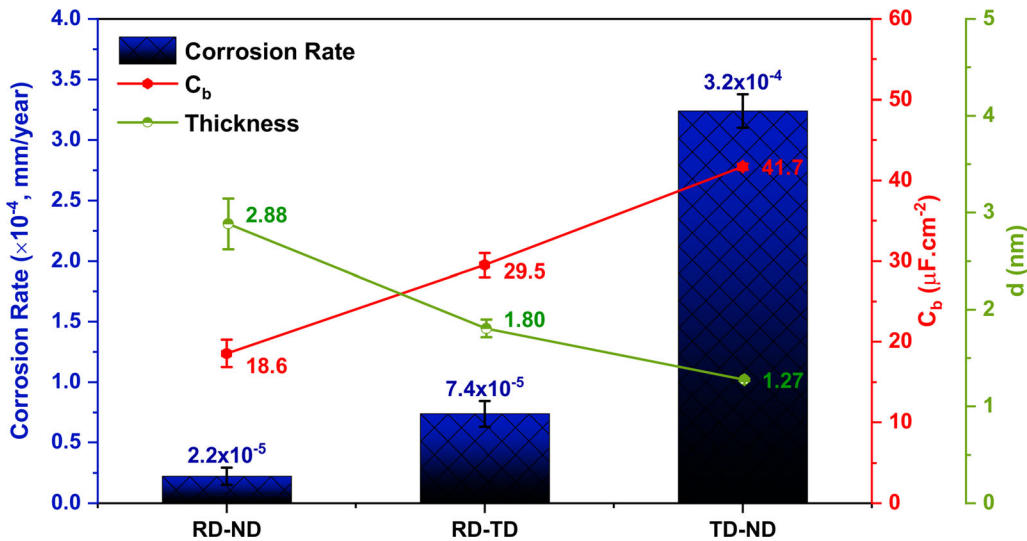


Fig. 12—Capacitance values for the barrier layer along with the calculated passive film thicknesses.

thicker passive layer formation on this surface. The thickness of the surface oxide layer can be influenced by the oxygen diffusion mechanism in  $\alpha$ -Ti as a predominant phase in Ti6Al4V alloy. The oxygen diffusion rate is mainly dependent on the planar atomic density of the diffusion. The close-packed  $\{0002\}$  planes are favorable to the diffusion of oxygen atoms, whereas the same does not apply for the  $\{11\bar{2}0\}$  and  $\{10\bar{1}0\}$  planes.<sup>[49]</sup> It is also worth noting that the oxygen diffusion pathways are symmetric at an equal distance on the basal planes that leads to the higher diffusion rate of oxygen.<sup>[49,50]</sup>

The passive layer formation and its related barrier properties can also be investigated from the surface energy perspective. As a general rule, areas on the surface with high free energy levels (e.g., grain boundaries) are more prone to corrosion.<sup>[51]</sup> Crystallographic planes with higher surface energy should also show lower corrosion resistance in comparison with planes of lower surface energy. Li *et al.*<sup>[52]</sup> used a surface model based on empirical electron theory (EET) to calculate the surface energy values for different crystallographic planes in materials with *hcp* structure. Their results showed that the surface energy for the  $\{0002\}$ ,  $\{10\bar{1}0\}$ , and  $\{11\bar{2}0\}$  planes of the  $\alpha$ -Ti phase are 8.764, 8.361, and 9.653 eV nm<sup>-2</sup>, respectively. These results may contrast with the corrosion rates presented in Table III and Figure 10. It is worth noting that for metallic systems of low corrosion rates, or systems having passivation behavior, the increase in active sites of the surface led to an increase in corrosion resistance.<sup>[53,54]</sup> The passive layer will preferentially grow at the active sites present on the surface. Accordingly, for the RD-ND surface in which some grains have their high energy  $\{11\bar{2}0\}$  plane parallel to the exposed surface, a thicker, denser, and more uniform passive layer is formed, as shown in Figure 12, which will reduce the corrosion rate.

## V. CONCLUSION

In the present study, the effect of crystallographic texture on the biocorrosion properties of the bimodal Ti6Al4V microstructure was investigated. To eliminate the impact of microstructure on corrosion performance, the same microstructure was developed on three orthogonal surfaces of a rectangular sample through heat treatment, wherein different crystallographic planes were placed parallel to different surfaces. A combination of microstructural examination, macrotexture investigation, and electrochemical measurements revealed that:

1. The same microstructural characteristics (*i.e.*, average primary  $\alpha$  grain size,  $\alpha$  grain size distribution, and equiaxed  $\alpha$  fraction) have been developed in the RD-TD, TD-ND, and RD-ND surfaces.
2. Applied heat treatment has led to texture transformation from  $11\bar{2}0\parallel\text{ND}$  fiber texture in as-received material to  $\{01\bar{1}2\}\bar{2}243$ ,  $\{01\bar{1}4\}\bar{2}3\bar{1}\bar{1}$ , and  $\{2\bar{2}31\}5\bar{4}\bar{1}\bar{1}$  components for heat-treated material.
3. From electrochemical measurements, crystallographic planes that are located in parallel to the surface have a significant impact on the corrosion properties of Ti6Al4V alloy in PBS solution. The  $\{0002\}$  planes exhibit relatively high corrosion resistance.
4. The  $\{11\bar{2}0\}$  planes show superior corrosion resistance in PBS solution. The existence of  $\{11\bar{2}0\}$  planes along with basal planes in parallel to the RD-ND surface decreased the corrosion rate to  $2.2 \times 10^{-5}$  mm/year.
5. The  $\{10\bar{1}0\}$  planes were the most prone to corrosion, whereby the TD-ND surface in which many grains have their  $\{10\bar{1}0\}$  planes in parallel to the surface showed the highest corrosion rate equal to  $3.2 \times 10^{-4}$  mm/year.



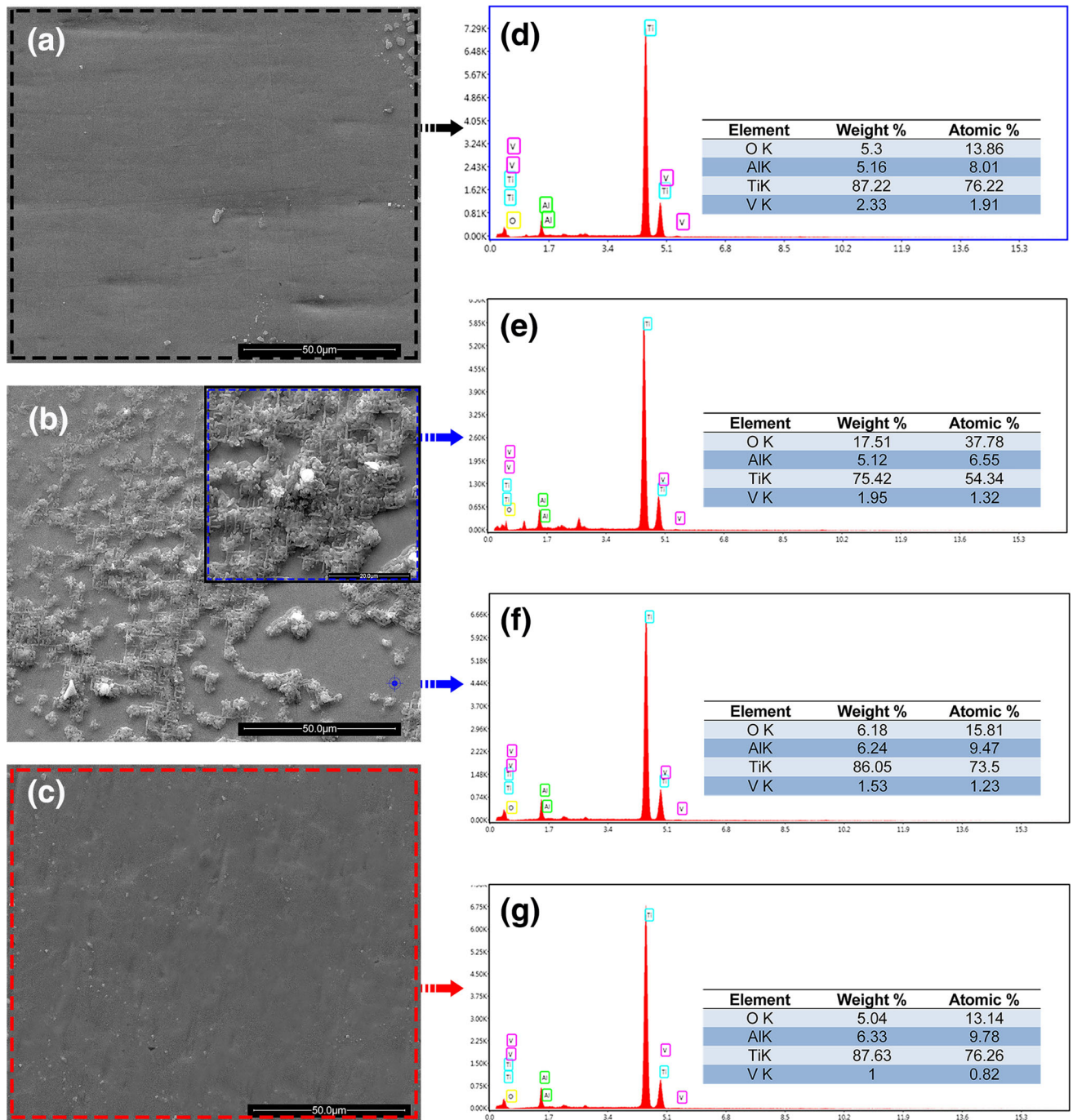


Fig. 13—(a to c) SEM micrographs and (d to g) the EDS plane scan for (a, d) the RD-TD surface, (b, e, f) TD-ND surface, and (c, g) RD-ND surface after the polarization test.

#### DATA AVAILABILITY

The raw/processed data required to reproduce these findings cannot be shared at this time as the data also form part of an ongoing study.

#### REFERENCES

1. A. Pandey, A. Awasthi, and K.K. Saxena: *Adv. Mater. Process. Technol.*, 2020, vol. 00, pp. 1–36.
2. R.I.M. Asri, W.S.W. Harun, M. Samykano, N.A.C. Lah, S.A.C. Ghani, F. Tarlochan, and M.R. Raza: *Mater. Sci. Eng. C*, 2017, vol. 77, pp. 1261–74.

3. Y. Ito, N. Hoshi, T. Hayakawa, C. Ohkubo, H. Miura, and K. Kimoto: *Mater. Sci. Eng. B*, 2019, vol. 245, pp. 30–36.
4. C. Xia, D. Cai, J. Tan, K. Li, Y. Qiao, and X. Liu: *ACS Biomater. Sci. Eng.*, 2018, vol. 4, pp. 3185–93.
5. M. Geetha, A.K. Singh, R. Asokamani, and A.K. Gogia: *Prog. Mater. Sci.*, 2009, vol. 54, pp. 397–425.
6. S. Bose, L.C. Pathak, and R. Singh: *Appl. Surf. Sci.*, 2018, vol. 433, pp. 1158–74.
7. O.S. Adesina, B.A. Obadele, G.A. Farotade, D.A. Isadare, A.A. Adediran, and P.P. Ikubanni: *J. Alloys Compd.*, 2020, vol. 827, art. no. 154245.
8. M.M.M. López, J. Fauré, M.I.E. Cabrera, and M.E.C. García: *Mater. Sci. Eng. B*, 2016, vol. 206, pp. 30–38.
9. M. Fazl, H.R. Salimijazi, and M. Shamanian: *ACS Appl. Mater. Interfaces*, 2018, vol. 10, pp. 15281–87.
10. L. Benea, A. Ravoivu, and J.P. Celis: *ACS Biomater. Sci. Eng.*, 2019, vol. 5, pp. 5925–34.
11. D.P. Perl and S. Moalem: *J. Alzheimer's Dis.*, 2006, vol. 9, pp. 291–300.
12. M.-J. Hosseini, F. Shaki, M. Ghazi-Khansari, and J. Pourahmad: *Metallomics*, 2013, vol. 5, pp. 152–66.
13. G.C. McKay, R. Macnair, C. Macdonald, and M.H. Grant: *Biomaterials*, 1996, vol. 17, pp. 1339–44.
14. M. Matsuo, S. Suwas, and R.K. Ray: *Crystallographic Texture of Materials*, Springer, New York, 2014.
15. V.A. Popovich, E.V. Borisov, A.A. Popovich, V.S. Sufiiarov, D.V. Masaylo, and L. Alzina: *Mater. Des.*, 2017, vol. 114, pp. 441–49.
16. C.Q. Li, D.K. Xu, S. Yu, L.Y. Sheng, and E.H. Han: *J. Mater. Sci. Technol.*, 2017, vol. 33, pp. 475–80.
17. A. Amininejad, R. Jamaati, and S.J. Hosseinipour: *Mater. Sci. Eng. A*, 2019, vol. 767, p. 138433.
18. X. Ren, Y. Huang, and Y. Liu: *J. Mater. Eng. Perform.*, 2018, vol. 27, pp. 3932–39.
19. F. Briffod, A. Bleuset, T. Shiraiwa, and M. Enoki: *Acta Mater.*, 2019, vol. 177, pp. 56–67.
20. W. Zhang, L. Tan, D. Ni, J. Chen, Y.C. Zhao, L. Liu, C. Shuai, K. Yang, A. Atrens, and M.C. Zhao: *J. Mater. Sci. Technol.*, 2019, vol. 35, pp. 777–83.
21. J. Fu, F. Li, J. Sun, K. Cui, X. Du, and Y. Wu: *J. Electroanal. Chem.*, 2019, vol. 841, pp. 56–62.
22. É. Martin, M. Azzi, G.A. Salishchev, and J. Szpunar: *Tribol. Int.*, 2010, vol. 43, pp. 918–24.
23. S. Bahl, P.L. Nithilaksh, S. Suwas, S.V. Kailas, and K. Chatterjee: *J. Mater. Eng. Perform.*, 2017, vol. 26, pp. 4206–16.
24. M. Amirnejad, M. Rajabi, and R. Jamaati: *Corros. Sci.*, 2021, vol. 179, art. no. 109100.
25. Z.X. Zhang, S.J. Qu, A.H. Feng, X. Hu, and J. Shen: *J. Alloys Compd.*, 2019, vol. 773, pp. 277–87.
26. J. Zhang, X. Li, D. Xu, and R. Yang: *Prog. Nat. Sci. Mater. Int.*, 2019, vol. 29, pp. 295–304.
27. M. Villa, J.W. Brooks, R.P. Turner, H. Wang, F. Boitout, and R.M. Ward: *Metall. Mater. Trans. B*, 2019, vol. 50B, pp. 2898–2911.
28. N. Stanford and P.S. Bate: *Acta Mater.*, 2004, vol. 52, pp. 5215–24.
29. W. Kou, Q. Sun, L. Xiao, and J. Sun: *J. Alloys Compd.*, 2020, vol. 820, art. no. 153421.
30. W. Simka, A. Sadkowski, M. Warczak, A. Iwaniak, G. Dercz, J. Michalska, and A. Maciej: *Electrochim. Acta*, 2011, vol. 56, pp. 8962–68.
31. X. Gai, Y. Bai, J. Li, S. Li, W. Hou, Y. Hao, X. Zhang, R. Yang, and R.D.K. Misra: *Corros. Sci.*, 2018, vol. 145, pp. 80–89.
32. I. Milošev, T. Kosec, and H.H. Strehblow: *Electrochim. Acta*, 2008, vol. 53, pp. 3547–58.
33. L. Wang, H. Yu, K. Wang, H. Xu, S. Wang, and D. Sun: *ACS Appl. Mater. Interfaces*, 2016, vol. 8, pp. 18608–19.
34. A.C. Hee, S.S. Jamali, A. Bendavid, P.J. Martin, C. Kong, and Y. Zhao: *Surf. Coat. Technol.*, 2016, vol. 307, pp. 666–75.
35. G. ASTM, G102, and G. ASTM: *G102-89, ASTM Int. West Conshohocken*, 2004, vol. 89, pp. 1–7.
36. A.C. Alves, F. Wenger, P. Ponthiaux, J.P. Celis, A.M. Pinto, L.A. Rocha, and J.C.S. Fernandes: *Electrochim. Acta*, 2017, vol. 234, pp. 16–27.
37. C.T. Kwok, P.K. Wong, F.T. Cheng, and H.C. Man: *Appl. Surf. Sci.*, 2009, vol. 255, pp. 6736–44.
38. H.A. Videla: *Manual of Biocorrosion*, CRC Press, Boca Raton, 1996.
39. D.J. Blackwood: *Electrochim. Acta*, 2000, vol. 46, pp. 563–69.
40. S.V. Gnedenkov and S.L. Sinebryukhov: *Elektrokhimiya*, 2005, vol. 41, pp. 963–71.
41. S.K. Poznyak, A.D. Lisenkov, M.G.S. Ferreira, A.I. Kulak, and M.L. Zheludkevich: *Electrochim. Acta*, 2012, vol. 76, pp. 453–61.
42. P. Qin, Y. Chen, Y.J. Liu, J. Zhang, L.Y. Chen, Y. Li, X. Zhang, C. Cao, H. Sun, and L.C. Zhang: *ACS Biomater. Sci. Eng.*, 2019, vol. 5, pp. 1141–49.
43. S. Ben Aoun, M. Bouklah, K.F. Khaled, and B. Hammouti: *Int. J. Electrochem. Sci.*, 2016, vol. 11, pp. 7343–58.
44. A. Wypych, I. Bobowska, M. Tracz, A. Opasinska, S. Kadlubowski, A. Krzywania-Kaliszewska, J. Grobelny, and P. Wojciechowski: *J. Nanomater.*, 2014, <https://doi.org/10.1155/2014/124814>.
45. M. Hoseini, A. Shahryari, S. Omanovic, and J.A. Szpunar: *Corros. Sci.*, 2009, vol. 51, pp. 3064–67.
46. G. Lütjering and J.C. Williams: *Titanium*, Springer, New York, 2007.
47. B. Pazhanivel, P. Sathiyaa, and G. Sozhan: *Opt. Laser Technol.*, 2020, vol. 125, art. no. 106017.
48. C. Leyens and M. Peters: *Titanium and Titanium Alloys: Fundamentals and Applications*, Wiley, New York, 2003.
49. H.G. Kim, T.H. Kim, and Y.H. Jeong: *J. Nucl. Mater.*, 2002, vol. 306, pp. 44–53.
50. H.H. Wu, P. Wisesa, and D.R. Trinkle: *Phys. Rev. B*, 2016, vol. 94, pp. 1–7.
51. Y.H. Ho, S.S. Joshi, T.C. Wu, C.M. Hung, N.J. Ho, and N.B. Dahotre: *Mater. Sci. Eng. C*, 2020, vol. 109, art. no. 110632.
52. B.Q. Fu, W. Liu, and Z.L. Li: *Appl. Surf. Sci.*, 2009, vol. 255, pp. 9348–57.
53. K.D. Ralston, N. Birbilis, and C.H.J.J. Davies: *Scr. Mater.*, 2010, vol. 63, pp. 1201–04.
54. W.T. Huo, L.Z. Zhao, W. Zhang, J.W. Lu, Y.Q. Zhao, and Y.S. Zhang: *Mater. Sci. Eng. C*, 2018, vol. 92, pp. 268–79.

**Publisher's Note** Springer Nature remains neutral with regard to jurisdictional claims in published maps and institutional affiliations.